Earth Science Informatics (2026) 19:79
https://doi.org/10.1007/s12145-026-02131-9

RESEARCH

Projection of extreme temperature and precipitation indices in the Moghan Plain, Iran, under CMIP6 scenarios

Pouya Allahverdipour[1,2] · **Yagob Dinpashoh**[1]

Received: 5 February 2026 / Accepted: 12 April 2026

Abstract
Climate change intensifies extreme weather events, threatening agriculture, water security, and socio-economic stability in semi-arid regions. This study projects 25 extreme climate indices for the Moghan Plain, Iran, using 1993–2014 data as baseline and bias-corrected outputs from eight CMIP6 models under SSP1-2.6 and SSP5-8.5 scenarios for 2021–2100. The three best-performing models (CanESM5, INM-CM5-0, and MPI-ESM1-2-LR) were selected for the ensemble based on superior skill scores. Trends were evaluated with the Mann–Kendall test and Sen's slope estimator, and uncertainty was quantified via bootstrap resampling. Results indicate a shift toward a hotter, more hydrologically stressed climate. Precipitation extremes intensify but become episodic: heavy rainfall indices (Rx1day + 5–6 mm, Rx5day + 1–3 mm, R95p + 7–8 mm, R99p + 2–3 mm, SDII, R10mm, R20mm) increase, while consecutive wet days (CWD) decline slightly (from 3.55 to 3.37–3.33 days/year) and consecutive dry days (CDD) lengthen significantly (from 60.77 to 61.72–66.15 days/year). Temperature extremes show strong warming: warm indices (TXx + 1.8 to + 4.5 °C, TNx + 1.1 to + 3.0 °C, SU25, TR20, TX90p, TN90p) rise markedly, cold indices (FD − 23 to − 36 days, ID, TX10p, TN10p, CSDI) decline sharply, and growing season length (GSL) extends (from 314.9 to 335.6–352.1 days). Diurnal temperature range (DTR) changes marginally. Uncertainty is higher for precipitation than temperature extremes and increases under SSP5-8.5. These shifts heighten risks of heat stress, drought, flash floods, and agro-climatic changes. Region-specific adaptation (e.g., integrated land-water management) is essential to enhance resilience in this vulnerable agricultural region.

Keywords Agriculture · Climate Change · Extreme Event · Sustainability · Trend Analysis · Water Resources

Introduction

Climatic extreme events are intricately linked to various sectors, including ecosystems and agriculture. These events, such as floods, prolonged periods of hot days, or days with heavy precipitation, are characterized by their rarity in terms of intensity and frequency. Changes in their intensity and duration can lead to significant environmental, agricultural, and economic losses. These extreme events exert a considerably greater impact than changes in climatic averages (Wei et al. 2023). Recent studies demonstrate that the frequency and severity of climatic extremes have escalated relative to historical data, with phenomena such as storms exhibiting increased intensity and droughts and frosts becoming more severe (Kuinkel et al. 2024; Elliot et al. 2025). These changes have adversely affected human livelihoods, agricultural productivity, and livestock production. Addressing the risks associated with climatic extremes necessitates foresight regarding future extreme events (IPCC 2013). Climate system models, which account for interactions between the atmosphere, lithosphere, and hydrosphere, serve as robust and essential tools for understanding current regional climates and predicting future climatic changes (Chen et al. 2019).

Numerous studies worldwide have investigated climate change and employed climate models to assess its impacts. The impact of climate change on extreme climatic events is particularly evident when models project a significant

Communicated by Hassan Babaie

✉ Pouya Allahverdipour
a.pouya1996@gmail.com; a.pouya@tabrizu.ac.ir;
pouyaallahverdi25@hacettepe.edu.tr

[1] Department of Water Engineering, Faculty of Agriculture, University of Tabriz, 29 Bahman Blvd, Tabriz 5166616471, Iran

[2] Department of Hydrogeological Engineering, Hacettepe University, Ankara, Türkiye

Published online: 25 April 2026

rise in both the frequency and upward trend of these events. Prominent research on the influence of climate change on the frequency of extreme climatic events includes studies by Grazzini et al. (2020) in Italy, Aleshina et al. (2021) in Russia, Shenoy et al. (2022) in the United States, and Zhu et al. (2024) in China. In northeast Iran, Kouzegaran et al. (2021) assessed extreme temperature indices for 1991–2016 and projected future trends based on CMIP5 scenarios, demonstrating rises in warm extreme indices and reductions in cold extreme indices across all scenarios. Sun et al. (2021) demonstrated that extreme precipitation events increased at two-thirds of global weather stations by 2018, with the proportion of stations exhibiting statistically significant upward trends exceeding what would be expected by chance across various continents. In South Korea, Felix et al. (2021) investigated trends in nine indices of extreme temperatures and eight indices of extreme precipitation in the upper Geum River basin over a 33-year period (1988–2020). Their results indicated heightened temperature intensity, decreased duration of cold spells, increased duration of warm spells, intensified precipitation, and prolonged intervals of consecutive wet and dry days. Fathian et al. (2023) investigated alterations in extreme temperature events across Iran during the baseline period of 1976–2005 and the projected period of 2025–2054, employing outputs from three regional climate models—namely, CCSM4, MPI-ESM-MR, and NORESM1-ME—under the RCP4.5 and RCP8.5 scenarios (CMIP5). Their analysis revealed upward trends in warm extreme indices (e.g., summer days and tropical days) and downward trends in cold extreme indices (e.g., frost days) at the majority of stations. In northwest Iran, Mohamadi et al. (2023) assessed trends in WSDI (warm spell duration) and CSDI (cold spell duration) using SSP scenarios and two optimal general circulation models (GCMs), projecting rising trends in WSDI and declining trends in CSDI at most stations. In China, Wei et al. (2023) forecasted extreme climatic events using the SSP scenarios. Projections suggested that the PTOT and Rx5day indices in northwest China would increase by over 30%, and the R20mm index would rise by approximately 4–5 days in southeast China under the SSP5-8.5 scenario. Temperature-related extreme indices were projected to increase over time, while TN10p was expected to decrease by more than 6% in eastern China. In the United States, Tefera et al. (2024) forecasted extreme climatic indices in Texas using data from 1985 to 2005 and CMIP5 scenarios for the near (2031–2060) and far (2070–2099) future. Their results projected increasing trends in temperature and temperature-related extreme indices under most scenarios, alongside reductions in the occurrence of cold nights and days, alongside increases in the occurrence of warm nights and days. Wang et al. (2025) investigated extreme heat and precipitation events in China using the CMIP6 models. Results indicated increasing intensity, frequency, and duration of extreme heat indices, with greater intensity at high latitudes and pronounced frequency/duration increases on the Tibetan Plateau. Extreme precipitation indices showed stronger increases in coastal areas, less in interiors, with notable rises on the Tibetan Plateau.

This study seeks to address the limited application of CMIP6 outputs and the scarcity of comprehensive climate research on the Moghan Plain. The objectives are threefold: (1) to systematically estimate 25 indices of extreme precipitation and temperature events using the RClimDex software package; (2) To investigate the historical patterns of these indices across the reference period of 1993–2014; and (3) To forecast their future trends until the close of the 21st century employing CMIP6 models under the SSP1-2.6 (optimistic) and SSP5-8.5 (pessimistic) scenarios. Through this approach, the study aims to improve understanding of climatic extremes in the Moghan Plain and to inform adaptive strategies for regional climate resilience.

Methodology

Geographical context of the study area

The Moghan Plain, spanning over 200,000 hectares, is located in northwest Iran, in the northern part of Ardabil Province, along the border with the Republic of Azerbaijan (Fig. 1). Renowned as a significant agricultural hub in Iran, the plain benefits from favorable farming conditions, including the presence of the Aras River, the Khoda Aarin and Aslanduz dams, fertile soils, and suitable temperature and humidity levels. This study utilizes climatic data from the Parsabad (Moghan) meteorological station, situated in the Moghan Plain, over 1993–2020. The Parsabad station is approximately located at 39°37’ N latitude, 47°53’ E longitude, and 72 m asl. The Moghan Plain experiences an annual mean of 261 mm of precipitation and a temperature of 15.5 °C, with 78 rainy days per year. According to the De Martonne index, the region is characterized as semi-arid.

Data Utilized

This study employs daily climatic data from the Parsabad meteorological station, including precipitation, mean minimum temperature, mean maximum temperature, and actual sunshine hours, to forecast future climatic conditions and calculate extreme climatic indices (Table 1). These data were sourced from the Islamic Republic of Iran Meteorological Organization (https://irimo.ir/eng/index.php).

Given that GCM simulations from the Sixth Assessment Report (AR6) extend up to 2014, the observational period up to this year was consistently adopted as the baseline period.

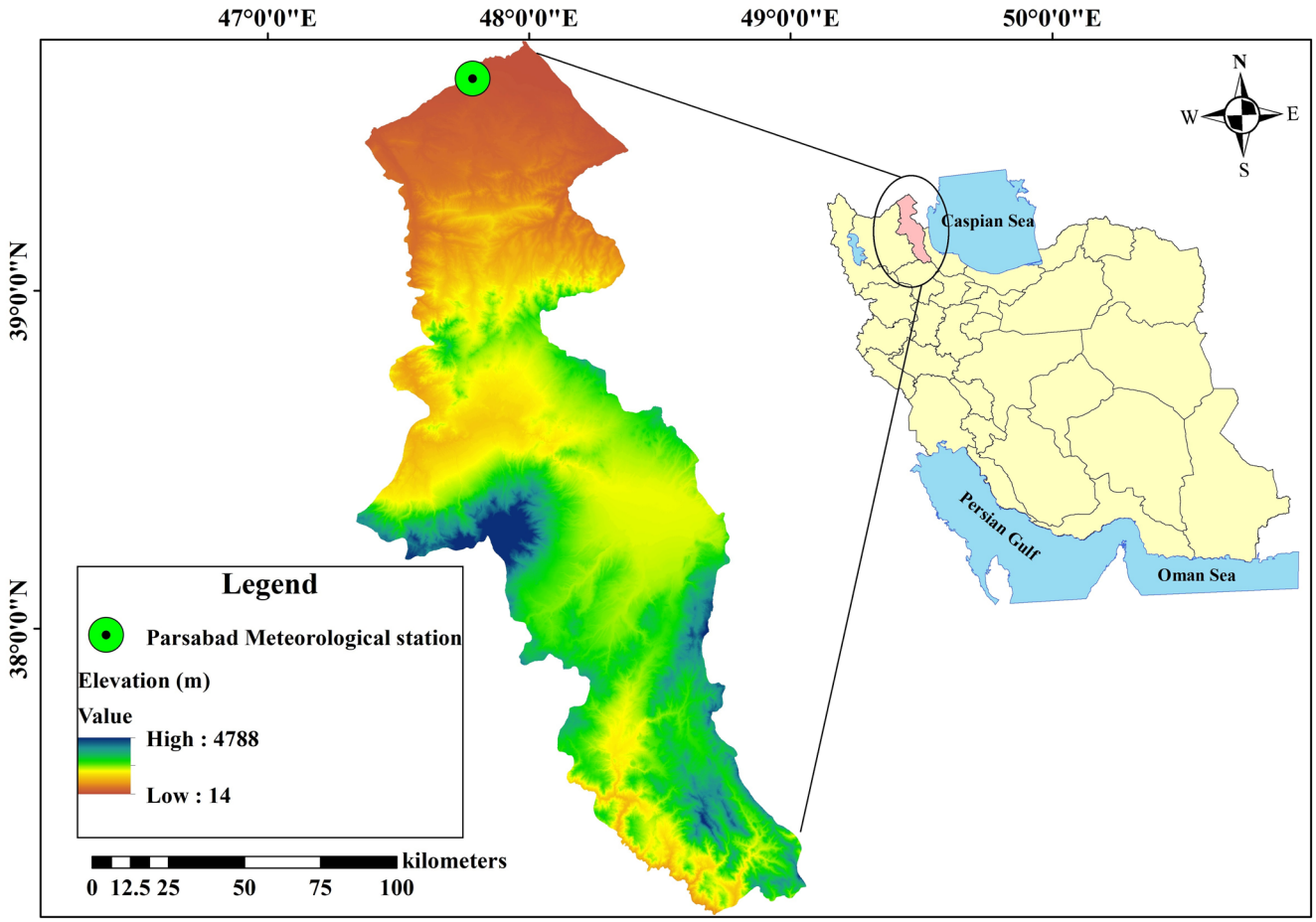

Fig. 1 Geographical Location of the Study Area, Parsabad meteorological Station in the Moghan Plain, Northwest Iran

Table 1 Statistical Characteristics of Daily Climatic Variables at the Parsabad Meteorological Station, Moghan Plain, Iran (1993–2020)

Statistics	T_{max} (°C)	T_{min} (°C)	Pre-cipitation (mm)	Sunshine (Hours)
Minimum	-3.2	-13.2	0	0
Maximum	44	27.4	65	14
Mean	21.2	10	1	6
Standard Deviation	10.1	8.2	3	4
Missing No. (%)	124 (1%)	336 (3%)	0	175 (2%)

Extreme climatic indices

Extreme climatic indices are defined as occurrences of climatic variables exceeding (or falling below) specific thresholds in a given region (IPCC 2013). Analyzing these indices and forecasting their future changes are critical for developing management strategies and adapting to future climatic shifts. In this study, 25 extreme climatic indices, as established by the Expert Team on Climate Change Detection, Monitoring, and Indices (ETCCDMI), were selected for analysis in the Moghan Plain for both the base period (1993–2014) and the future period (2015–2100). The formulation of these indices originated from a cooperative initiative led by the World Meteorological Organization (WMO), encompassing the Commission for Climatology (CCL), the Climate Variability and Predictability (CLIVAR) program, the World Climate Research Programme (WCRP), and the Expert Team on Climate Change Detection, Monitoring, and Indices (ETCCDMI) (Karl et al. 1999; Peterson et al. 2001). This collaboration established standardized definitions and methodologies indices of extreme temperature and precipitation events (Tables 2 and 3). All percentile-based indices are calculated using fixed thresholds derived from the baseline period. These thresholds are then consistently applied to both the historical and future periods to ensure temporal consistency and comparability of extreme climate indices.

The *RClimDex software package*, implemented in the *R programming language*, was used to calculate and estimate these extreme climatic indices (Zhang et al. 2004).

Table 2 Extreme Precipitation Indices Provided by ETCCDMI (Karl et al. 1999)

Row	Index	Name of Index	Unit
1	Rx1day	Maximum 1-day precipitation	mm
2	Rx5day	Maximum 5-day precipitation	mm
3	SDII	Simple daily intensity index	mm per day
4	R10mm	Annual count of days when precipitation ≥ 10 mm	day
5	R20mm	Annual count of days when precipitation ≥ 20 mm	day
6	CDD	Maximum number of consecutive days with precipitation < 1 mm	day
7	CWD	Maximum number of consecutive days with precipitation ≥ 1 mm	day
8	R95p	Annual total precipitation from days > 95th percentile	mm
9	R99p	Annual total precipitation from days > 99th percentile	mm

Coupled model intercomparison project phase 6 (CMIP6) scenarios

This study leverages outputs from 9 General Circulation Models (GCMs) under the IPCC's Sixth Assessment Report (CMIP6) to project daily minimum temperature, maximum temperature, and precipitation for the Moghan Plain, northwest Iran, from 2021 to 2100. To mitigate the influence of internal climate variability inherent in individual models, the multi-model ensemble mean was computed to evaluate changes in temperature and precipitation (Chen et al. 2019; Yu et al. 2020). This approach enhances the robustness of the analysis by averaging outputs across multiple General Circulation Models (GCMs), thereby reducing the impact of model-specific variability and providing a more reliable assessment of projected climatic trends (Wang et al. 2025). The projections are based on two Shared Socioeconomic Pathways (SSPs): SSP1-2.6, representing an optimistic scenario with strong climate policies that limit warming to approximately 2 °C, and SSP5-8.5, representing a pessimistic scenario characterized by high greenhouse gas emissions and minimal mitigation efforts. To improve spatial resolution for regional climate impact assessments, the LARS-WG was used to downscale the coarse outputs of General Circulation Models (GCMs). LARS-WG generates synthetic daily weather data by integrating historical observations with GCM projections, capturing interactions between the atmosphere, lithosphere, and hydrosphere. The LARS-WG model downscales climate projections from GCMs by incorporating local-scale changes in mean climate, variability, and extreme events. This is achieved by adjusting the statistical distributions of weather variables at each site using

Table 3 Extreme Temperature Indices Provided by ETCCDMI (Karl et al. 1999)

Row	Type	Index	Name of Index	Unit
1	Warm	SU25	Annual count when daily max temperature > 25 °C	day
2		TR20	Annual count when daily min temperature > 20 °C	day
3		TX90p	Percentage of time when daily maximum temperature > 90th percentile	day
4		TN90p	Percentage of time when daily minimum temperature > 90th percentile	day
5		WSDI	Annual count when at least 6 consecutive days of max temperature > 90th percentile	day
6		TXx	Monthly highest value of daily maximum temperature	°C
7		TNx	Monthly highest value of daily minimum temperature	°C
8	Cold	FD	Annual count when daily minimum temperature < 0 °C	day
9		ID	Annual count when daily maximum temperature < 0 °C	day
10		TXn	Monthly lowest value of daily maximum temperature	°C
11		TNn	Monthly lowest value of daily minimum temperature	°C
12		TX10p	Percentage of time when daily maximum temperature < 10th percentile	day
13		TN10p	Percentage of time when daily minimum temperature < 10th percentile	day
14		CSDI	The number of days when daily minimum temperature is below the 10th percentile of the baseline period for at least six consecutive days	day
15	Difference	DTR	Annual mean difference between daily max and min temperature	°C
16	Duration	GSL	Annual count between first span of at least 6 days with daily mean temperature > 5 °C and first span after 1 July of 6 days with daily mean temperature < 5 °C	day

delta-changes derived from the GCM outputs (Semenov 2021). The performance of the LARS-WG weather generator in reproducing observed climate characteristics was evaluated during the baseline period using statistical comparison of monthly distributions of daily precipitation, minimum temperature (Tmin), and maximum temperature (Tmax). The Kolmogorov–Smirnov (KS) test results indicated no significant differences (p-value > 0.05) between observed and simulated data for all months and variables, demonstrating the capability of LARS-WG to reliably

reproduce the statistical properties and extremes of the observed climate. Detailed monthly statistics are provided in Supplementary Table S1.

GCMs, critical for global climate research, simulate climatic variables across past, present, and future periods, accounting for varying GHG concentrations. The CMIP6 models, an advancement over previous iterations, feature increased vertical layers for improved stratospheric simulation accuracy (Chen et al. 2020). The 8 GCMs were selected for their diverse modeling approaches, addressing uncertainties in model structure and parameterization. Based on their performance over the Moghan Plain, Iran, climate sensitivity, and the distribution of GCMs, a subset of the three best-performing GCMs—CanESM5, INM-CM5-0, and MPI-ESM1-2-LR—was selected. These models are evenly distributed within the CMIP6 ensemble, capturing the uncertainty in future climate projections. Using this subset considerably reduces computational time for impact assessment studies while still allowing an explicit estimation of uncertainties in impacts arising from GCM-related climate projection variability (Semenov et al. 2025). Specifications and developing institutions of the selected models are provided in Table 4.

The SSP1-2.6 scenario represents strong mitigation and sustainable development, resulting in reduced radiative forcing by 2100, whereas SSP5-8.5 corresponds to a fossil-fuel-intensive pathway associated with substantial warming (Dinpashoh and Allahverdipour 2025). By analyzing temperature and precipitation under these scenarios, the study provides insights for agriculture, water management, and policy planning in the Moghan Plain. The downscaled data support region-specific strategies to mitigate the impacts of climate extremes, highlighting the importance of robust climate policies to minimize adverse effects under high-emission scenarios.

Table 4 Characteristics of the GCMs used in this study

No	Model	Institutions	Country	Horizontal resolution (lon × lat)
1	ACCESS-ESM1-5	Australian Community Climate	Australia	192 × 145
2	CanESM5	Canadian Centre for Climate Modelling and Analysis, Environment and Climate Change Canada	Canada	128 × 64
3	CMCC-ESM2	Euro-Mediterranean Centre on Climate Change-Earth System Mode	Europe	362 × 292
4	GFDL-ESM4	Administration, Geophysical Fluid Dynamics Laboratory	USA	288 × 180
5	INM-CM5-0	Institute for Numerical Mathematics, Russian Academy of Science, Moscow	Russia	180 × 120
6	MIROC6	Japan Agency for Marine- Earth Science and Technology	Japan	256 × 128
7	MPI-ESM1- 2-LR	Max Planck Institute for Meteorology	Germany	384 × 192
8	MRI-ESM2-0	Meteorological Research Institute	Japan	320 × 160

Bias Correction of GCM Outputs

To reduce systematic biases in the downscaled GCM outputs, an Empirical Quantile Mapping (EQM) bias correction was applied to daily precipitation, maximum temperature (T_{max}), and minimum temperature (T_{min}) variables, as this is one of the most reliable methods for bias correction (Rajkumar et al. 2026). EQM is a non-parametric approach that maps the cumulative distribution function (CDF) of model simulations to that of observed data during the baseline period (Sarkar and Maity 2022; Choudhary et al. 2025).

For each grid cell and calendar month, the bias-corrected value (P_{cor}) is derived as Eq. (1) (Cannon et al. 2015):

$$P_{cor} = F_{obs}^{-1}(F_{mod}(P_{raw})) \quad (1)$$

where, P_{raw} is the raw GCM output, F_{mod} is the CDF of the model data during the baseline period, and F_{obs}^{-1} is the inverse CDF of the observed data. Supplementary Figs. S1-S3 show the probability density functions of precipitation, minimum temperature, and maximum temperature before and after bias correction, demonstrating improved agreement with observations for both mean values and extremes (Cannon et al. 2015).

Trend analysis

The aim of the trend analysis is to identify whether a time series exhibits a consistent increasing or decreasing pattern.

For hydrological and meteorological variables, assumptions such as normality, stationarity, and independence of the observation series do not hold. Therefore, non-parametric methods are employed. Non-parametric methods are less sensitive to extreme values compared to parametric methods, and these types of tests can be applied without considering whether the trend in the data is linear or nonlinear. The non-parametric MK test was introduced by Mann (1945) and further developed by Kendall (1948).

If the number of time series data points in the period under investigation is n, the statistic S is initially calculated from Eq. (2):

$$S = \sum_{k=1}^{n-1} \sum_{j=k+1}^{n} sgn\left(x_j - x_k\right) \tag{2}$$

where x_j and x_k are the *j-th* and *k-th* data values, respectively, and $sgn\left(\theta\right)$ is the sign function defined by Eq. (3):

$$sgn\left(\theta\right) = \begin{cases} +1 & if\ \left(x_j - x_k\right) > 0 \\ 0 & if\ \left(x_j - x_k\right) = 0 \\ -1 & if\ \left(x_j - x_k\right) < 0 \end{cases} \tag{3}$$

Next, the variance of S, denoted as $Var\left(s\right)$ is calculated from Eq. (4):

$$Var\left(s\right) = \frac{n\left(n-1\right)\left(2n+5\right) - \sum_{i=1}^{P} t_i\left(t_i-1\right)\left(2t_i-5\right)}{18} \tag{4}$$

where t_i represents the number of identical data points in the *i-th* group, and P denotes the total number of groups with tied observations. The Mann-Kendall (MK) test statistic Z is then calculated using Eq. (5):

$$Z = \begin{cases} \frac{S-1}{\sqrt{Var(s)}} & if\ S > 0 \\ 0 & if\ S = 0 \\ \frac{S+1}{\sqrt{Var(s)}} & if\ S < 0 \end{cases} \tag{5}$$

A positive value of Z indicates an increasing trend, while a negative value indicates a decreasing trend in the data. Additionally, α is the significance level considered for this test. The null hypothesis (H_0), which assumes no trend, is not rejected if the absolute value of the calculated Z statistic is smaller than the critical Z value from the standard normal distribution at the chosen significance level (α/2 for a two-tailed test). Otherwise, H_0 is rejected and the alternative hypothesis, indicating the presence of a significant trend, is accepted (Mann 1945; Kendall 1948). In this study, the trend was evaluated at a 5% significance level ($p < 0.05$).

In trend studies, the presence of significant autocorrelation coefficients can lead to misleading results. Therefore, to eliminate the effects of significant autocorrelation coefficients from the time series, the modified MK test was employed (Hamed and Rao 1998). According to this method, the autocorrelation coefficient of order k (r_k) is first obtained from Eq. (6):

$$r_k = \frac{\frac{1}{n-k}\sum_{i=1}^{n-k}\left(x_i - \bar{x}\right)\left(x_{i+k} - \bar{x}\right)}{\frac{1}{n}\sum_{i=1}^{n}\left(x_i - \bar{x}\right)^2} \tag{6}$$

where n is the number of data points and k is the lag order.

where n represents the total number of data points and k denotes the lag order. If the condition $\frac{1-Z_{1-\alpha/2}\sqrt{n-k-1}}{n-k} \le r_k \le \frac{1+Z_{1-\alpha/2}\sqrt{n-k-1}}{n-k}$ is satisfied, the data series is assumed to be independent at the α level, and calculations are performed using the original MK test. However, if the autocorrelation coefficient of order k falls outside this range, the modified variance, denoted as $Var\left(s\right)^*$, is first calculated using the Eq. (7):

$$Var\left(s\right)^* = Var\left(s\right) x \frac{n}{n^*} \tag{7}$$

where the ratio $\frac{n}{n^*}$ is derived from Eq. (8):

$$\frac{n}{n^*} = 1 + \frac{2}{n\left(n-1\right)\left(n-2\right)} \sum_{k=1}^{n-1} \left(n-i\right)\left(n-i-1\right)\left(n-i-2\right) r_k \tag{8}$$

Subsequently, the computed $Var\left(s\right)^*$ is substituted in place of $Var\left(s\right)$, and the statistic Z is recalculated. Finally, the significance of the trend is assessed (Hamed and Rao 1998; Dinpashoh et al. 2011).

To calculate the magnitude of trend slope, the non-parametric Sen's slope estimator was employed. This method is especially valuable in disciplines such as environmental science, hydrology, and climatology, where the data may not satisfy the assumptions required for parametric tests, including normality and homoscedasticity. The Sen's slope estimator (Sen 1968) can be described by the Eq. (9):

$$s = Median\left[\frac{X_j - X_i}{j - i}\right] \quad , \quad \left(j > i\right) \tag{9}$$

where s represents the slope estimator of the trend line, and X_i and X_j are the observed values at indices i and j in the dataset, respectively. A positive value of s indicates an upward slope of the trend line, while a negative value signifies a downward slope in the data series.

A positive s value indicates an upward trend, whereas a negative s value corresponds to a downward trend in the data series.

Due to the large number of simultaneous statistical tests performed on the 25 ETCCDI indices, the risk of false positive trend detection increases substantially; therefore, the Benjamini–Hochberg false discovery rate (FDR) procedure was applied at $q = 0.05$ to control the expected proportion of erroneous rejections. q-values represent the false discovery rate (FDR)-adjusted p-values. They are obtained by applying the Benjamini–Hochberg procedure (Benjamini and Hochberg 1995) to control the expected proportion of false positives (Type I errors) when performing multiple hypothesis tests simultaneously (Haynes 2013).

In contrast to the conventional p-value (which controls the probability of a Type I error for a single test), the q-value accounts for the fact that 25 ETCCDI indices were tested at the same time. A q-value of 0.03, for example, means that among all tests declared significant at $q \leq 0.03$, we expect at most 3% to be false positives. The procedure works as follows (Haynes 2013):

1. Compute the original (uncorrected) p-values from the Mann–Kendall test for all 25 indices.
2. Rank the p-values in ascending order ($p(1) \leq p(2) \leq \ldots \leq p(25)$).
3. For each ranked p-value p(i), calculate the q-value as: $q(i) = \min((p(i)) \times m / i, q(i-1))$, where $m = 25$ (number of tests), starting from the largest p-value and moving backward.
4. Trends with $q < 0.05$ are considered statistically significant after FDR correction.

Trends are classified as (Haynes 2013):

- Significant after FDR correction — $q < 0.05$.
- Significant before FDR correction only — $p < 0.05$ but $q \geq 0.05$.
- Not significant — $p \geq 0.05$ (and thus $q \geq 0.05$).

Results and discussion

Ranking of CMIP6 models

Model performance in reproducing observed ETCCDI indices during the baseline period (1993–2014) was evaluated using RMSE, MAE, and PBIAS as primary metrics. The RMSE values, broken down separately for groups of indices with identical units, are presented in Figs. 2, 3 and 4, while the complete values of RMSE, MAE, and PBIAS for all models and all indices are provided in Supplementary Table S2 to avoid excessive length in the main text. In addition, the boxplot distributions of all observed and model-simulated indices during the baseline period, illustrating their statistical dispersion and consistency across models, are provided in Supplementary Fig. S4.

The multi-model ranking (Fig. 5) shows clear differences in performance across indices and models. CanESM5 achieved the best overall performance with the lowest sum of ranks (90) and mean rank of 3.56, followed by INM-CM5-0 (sum = 96, mean rank = 3.93) and MPI-ESM1-2-LR

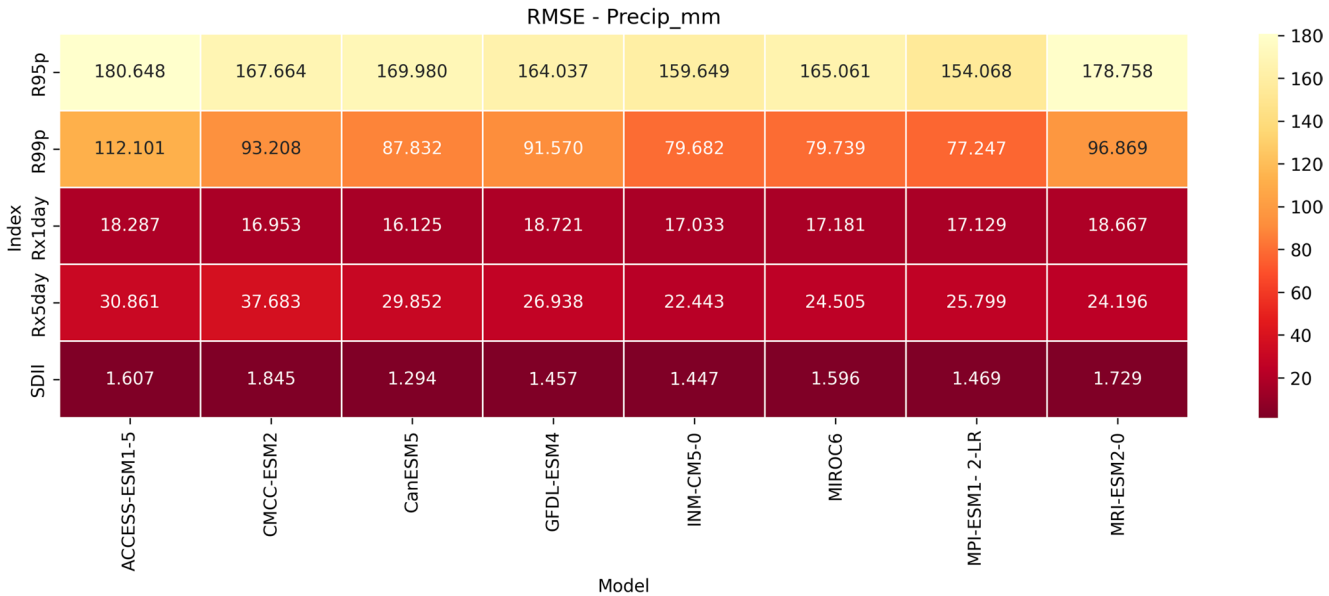

Fig. 2 Root Mean Square Error (RMSE) of the eight CMIP6 models in simulating precipitation-related ETCCDI indices compared to observations during the baseline period (1993–2014). Lower RMSE values indicate better model performance

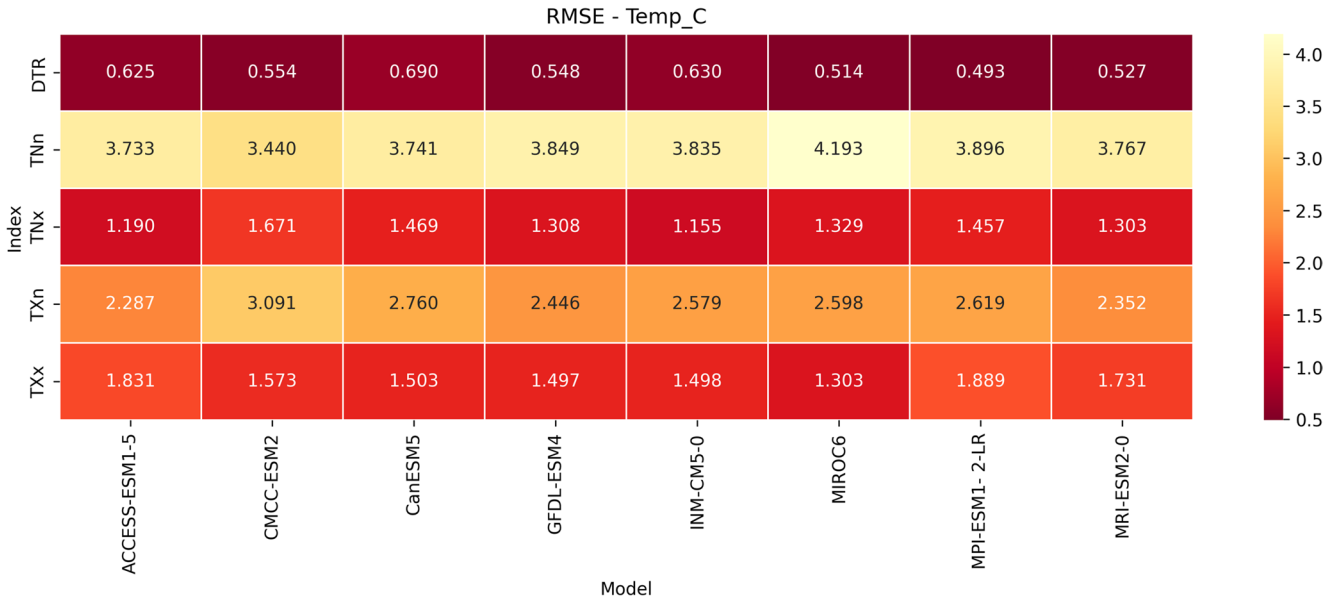

Fig. 3 As in Fig. 2 but for temperature-related ETCCDI indices

(sum = 98, mean rank = 4.04). These three models consistently ranked among the top performers across both temperature and precipitation extremes.

In contrast, CMCC-ESM2 exhibited the weakest overall performance (sum of ranks = 132, mean rank = 5.11), particularly in precipitation-related indices such as R95p, R99p, and Rx5day, where it ranked 7th or 8th in most cases. ACCESS-ESM1-5 and MRI-ESM2-0 showed balanced but intermediate performance (mean ranks 4.83 and 4.97, respectively), with strengths in temperature extremes (e.g., TXx and TNx) but relatively poorer performance in some precipitation indices.

The heatmap (Fig. 5) highlights structural differences: CanESM5 and INM-CM5-0 dominate in warm extremes (TXx, TNx, SU25) and growing season length (GSL), while MPI-ESM1-2-LR and GFDL-ESM4 perform better in cold extremes (FD, ID, TNn). Precipitation indices show greater inter-model spread, with no single model consistently excelling across all precipitation metrics.

The ranking results (Fig. 5; Table 5) demonstrate that CanESM5, INM-CM5-0, and MPI-ESM1-2-LR provide the most skillful representation of the observed ETCCDI indices in the study region during the baseline period. The superior performance of these three models in extremes (e.g., high ranks in TXx, TNx, Rx5day, and GSL) supports their selection as the final ensemble members for future projections. Conversely, CMCC-ESM2's consistently poor performance in precipitation extremes (high ranks in R95p, R99p, Rx1day) suggests structural limitations in its representation of convective and orographic precipitation processes, which is a known issue in some CMIP6 models. The greater inter-model spread in precipitation indices compared to temperature indices reflects the higher uncertainty and complexity in simulating extreme precipitation events, particularly in regions with complex topography like the study area. This spread underscores the importance of using a multi-model ensemble rather than relying on a single GCM for impact assessments.

Effects of climate change on extreme climate indices

Table 6 presents the projected multi-year mean values of the 25 ETCCDI extreme climate indices for the Moghan Plain under the baseline period (1993–2014) and the two future periods (2015–2100) for the SSP1-2.6 and SSP5-8.5 scenarios.

Precipitation extremes show a clear tendency toward intensification and greater temporal concentration. The mean values of most heavy precipitation indices (Rx1day, Rx5day, SDII, R10mm, R20mm, R95p, and R99p) are projected to increase under both scenarios, with generally larger changes under SSP5-8.5. At the same time, the mean consecutive wet days (CWD) index is projected to decrease slightly from 3.55 days in the baseline to 3.37 and 3.33 days under SSP1-2.6 and SSP5-8.5, respectively, while the mean consecutive dry days (CDD) index is projected to rise from 60.77 days to 61.72 and 66.15 days, respectively. This combination indicates a future climate with more intense but less frequent precipitation events and longer dry spells, which is consistent with thermodynamic arguments for increased moisture-holding capacity and the expected poleward expansion of subtropical dry zones.

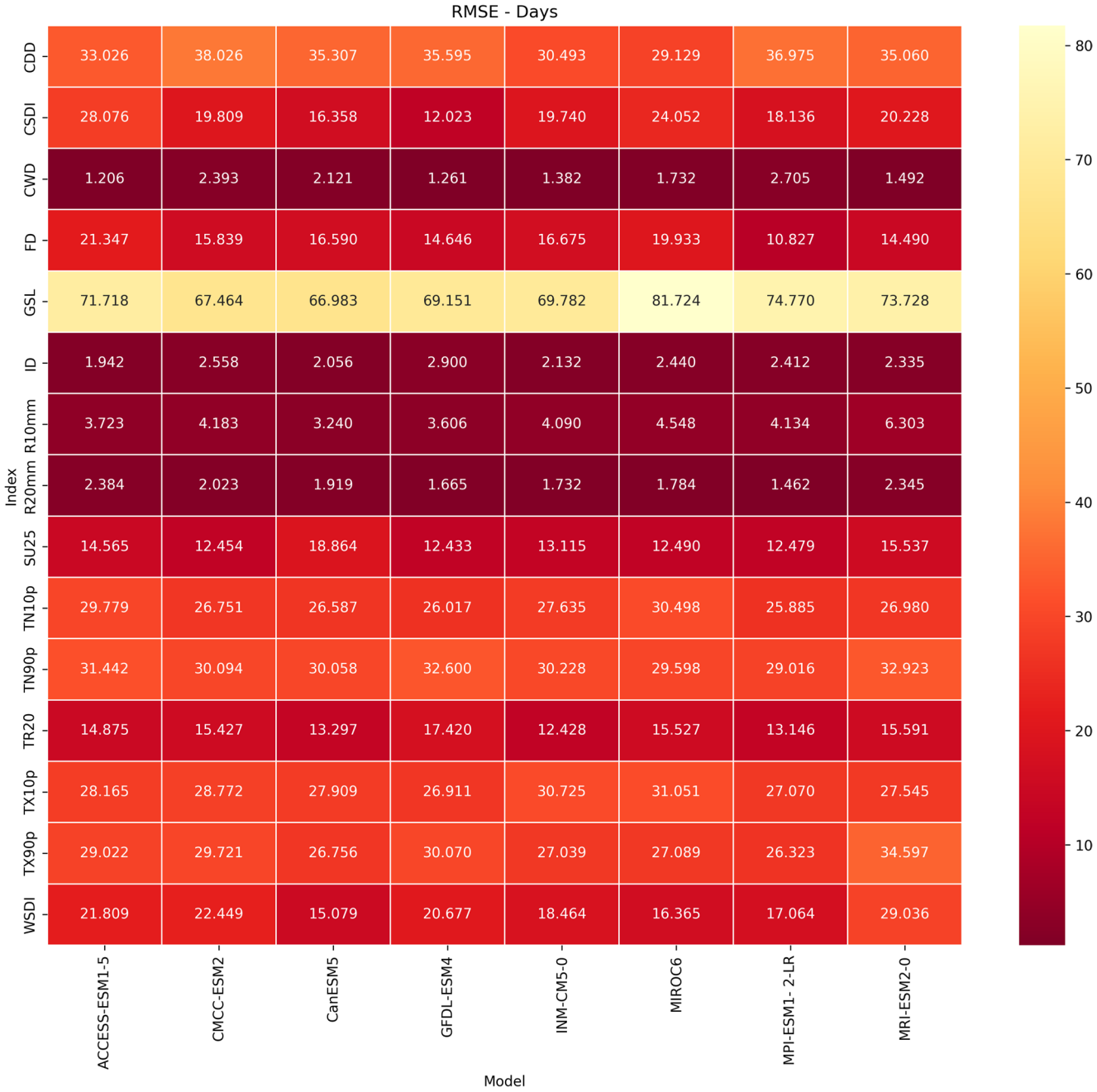

Fig. 4 As in Fig. 2 but for day-based ETCCDI indices

Temperature extremes exhibit a very strong warming signal, particularly in the warm tail of the distribution. Warm spell duration (WSDI) is the only warm extreme index projected to decrease (from 1.82 days to 0.20 and 0.48 days under SSP1-2.6 and SSP5-8.5, respectively), most likely due to the very large baseline values in certain years being replaced by a more uniformly warm climate. All other warm indices (TXx, TNx, SU25, TR20, TX90p, TN90p) increase substantially, with changes under SSP5-8.5 being markedly larger than under SSP1-2.6.

The cold extremes (FD, ID, TX10p, TN10p, CSDI) decrease dramatically, with the largest relative reductions occurring under the high-emission scenario. For example, the mean frost days (FD) index is projected to fall from 49.5 days to 26.1 and 13.9 days under SSP1-2.6 and SSP5-8.5, respectively. The diurnal temperature range (DTR) shows only a marginal increase (<0.5 °C) under both scenarios, suggesting that minimum temperatures are warming at a rate comparable to or slightly faster than maximum temperatures. The growing season length (GSL) is projected to

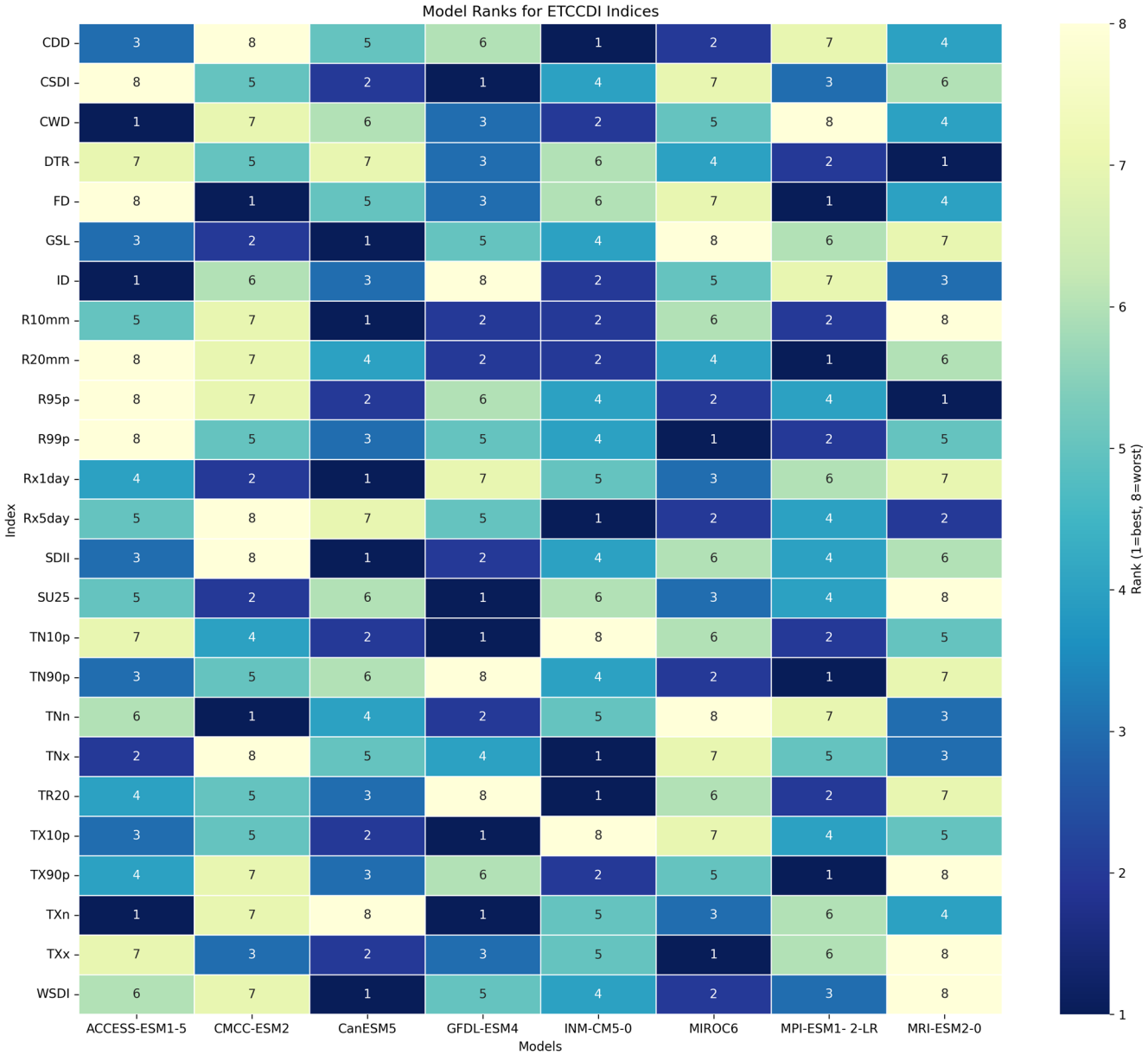

Fig. 5 Heatmap of model ranks across 25 ETCCDI indices during the baseline period (1993–2014). Lower rank (blue) indicates better performance

Table 5 Model overall ranks across 25 ETCCDI indices during the baseline period (1993–2014). Lower rank indicates better performance

Index	ACCESS-ESM1-5	CMCC-ESM2	CanESM5	GFDL-ESM4	INM-CM5-0	MIROC6	MPI-ESM1- 2-LR	MRI-ESM2-0
Overall Rank	6	8	1	4	2	5	3	7

lengthen significantly from 314.9 days to 335.6 and 352.1 days under SSP1-2.6 and SSP5-8.5, respectively, which may benefit certain agricultural activities in the short to medium term but will also increase exposure to heat stress during critical crop growth stages.

Overall, the projected changes point to a future climate in the Moghan Plain characterized by more intense precipitation extremes, longer dry periods, substantially fewer cold days, and a marked intensification of warm extremes, especially under the high-emission SSP5-8.5 pathway. These shifts are expected to have important implications for water resources, agriculture, ecosystems, and human health in the region.

Trend analysis

The results of the Mann–Kendall trend analysis and Sen's slope estimates for the baseline period and future

Table 6 Means of Extreme Precipitation and Temperature Indices for the Moghan Plain During the Baseline Period (1993–2014) and Future Period (2015–2100) Under SSP1-2.6 and SSP5-8.5 Scenarios

Row	Index	Unit	1993–2014	2015–2100 (SSP1-2.6)	2015–2100 (SSP5-8.5)
1	Rx1day	mm	28.25	33.88	33.72
2	Rx5day	mm	41.76	43.06	44.28
3	SDII	mm per day	5.94	7.23	7.14
4	R10mm	day	7.86	9.74	9.51
5	R20mm	day	1.91	2.94	2.63
6	CDD	day	60.77	61.72	66.15
7	CWD	day	3.55	3.37	3.36
8	R95p	mm	58.81	66.53	66.24
9	R99p	mm	17.38	19.99	20.28
10	SU25	day	144.73	163.07	178.71
11	TR20	day	45.32	63.58	88.78
12	TX90p	day	9.51	9.98	10.22
13	TN90p	day	9.08	9.83	10.23
14	WSDI	day	1.82	0.20	0.48
15	TXx	°C	38.7	40.52	43.18
16	TNx	°C	25.49	26.57	28.52
17	FD	day	49.5	26.10	13.92
18	ID	day	1.09	0.09	0.07
19	TXn	°C	0.37	1.78	3.60
20	TNn	°C	-8.05	-6.86	-4.66
21	TX10p	day	11.03	9.96	10.04
22	TN10p	day	10.67	9.87	10.03
23	CSDI	day	2.59	0.08	0.08
24	DTR	°C	11.08	11.37	11.53
25	GSL	day	314.86	335.60	352.08

projections under the SSP1–2.6 and SSP5–8.5 scenarios are presented in Figs. 6 and 7, while detailed numerical values (including Z statistics, Sen's slopes, p-values, q-values, and autocorrelation metrics) are provided in Supplementary Tables S3-S5 to avoid excessive length in the main manuscript.

The baseline period (1993–2014) shows limited evidence of statistically significant trends in extreme climate indices. Most precipitation-related indices, including Rx1day, Rx5day, R95p, and R99p, do not exhibit significant trends, indicating relative stability in extreme precipitation characteristics during the observational period. The only marginal signal is observed in SDII, which shows a weak increasing trend significant at the 5% level ($p < 0.05$), although this significance disappears after FDR correction. In contrast, temperature extremes show a more distinct signal, with TN90p (warm nights) exhibiting a strong and statistically significant increasing trend that remains robust after FDR correction. This indicates that nighttime warming is already a detectable feature of the regional climate, while other indices of temperature extremes show non-significant tendencies consistent with gradual warming.

In future projections, a clear intensification of trends is observed, particularly under the SSP1–2.6 scenario. Several precipitation indices, including Rx1day, Rx5day, SDII, and R95p, show statistically significant increasing trends that remain robust after

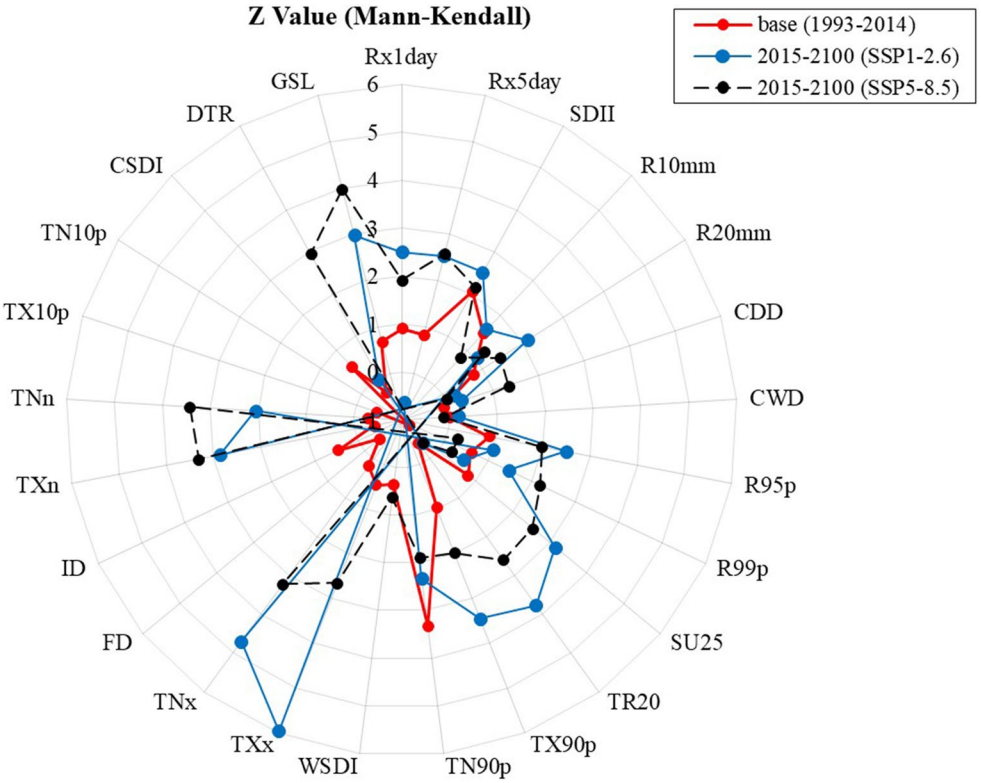

Fig. 6 Extreme Climatic Indices Changes Trends for the Moghan Plain During the Baseline Period (1993–2014) and Future Period (2015–2100) Under SSP1-2.6 and SSP5-8.5 Scenarios (at the 5% significancy level)

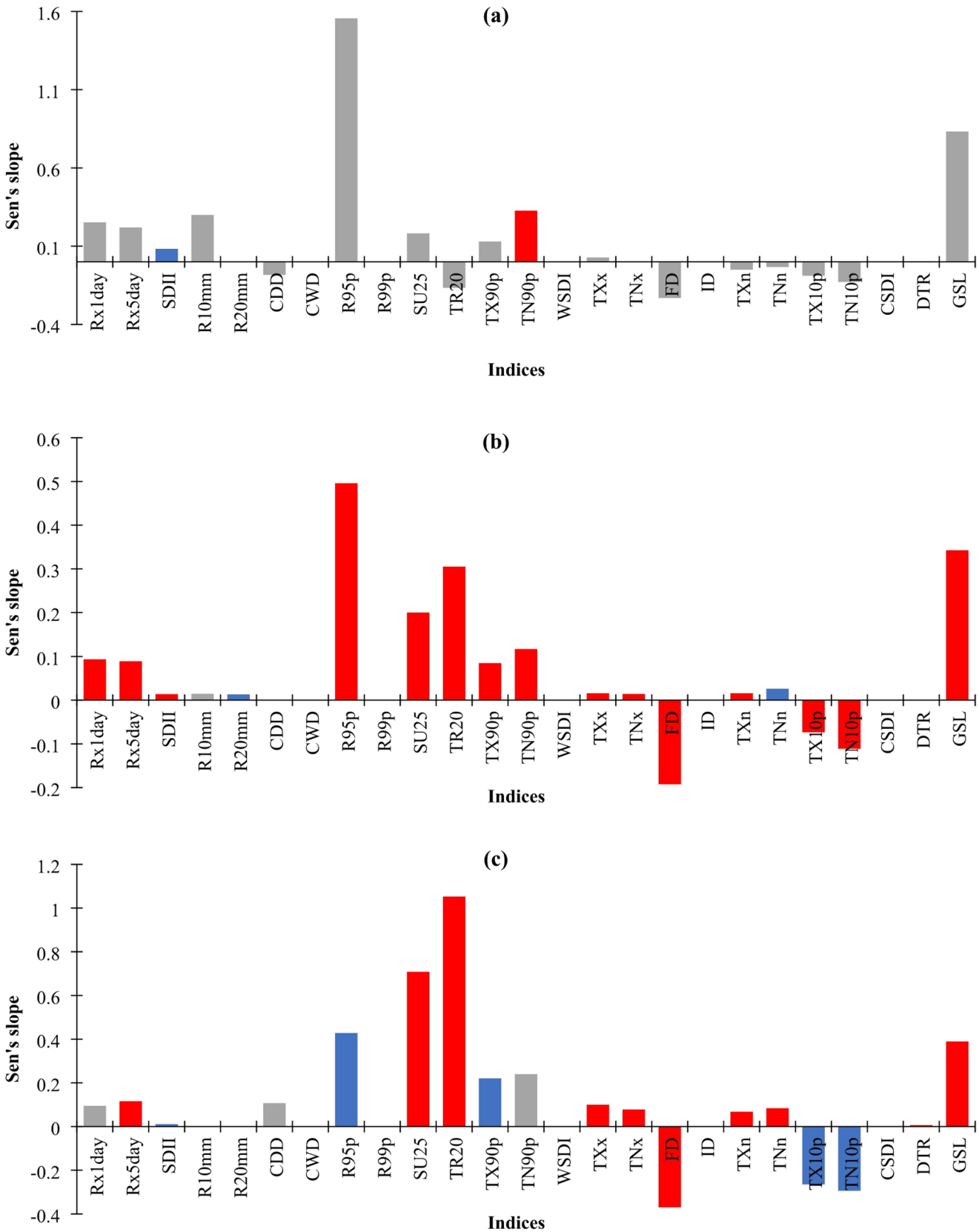

Fig. 7 Sen's Slope of Extreme Indices for the Moghan Plain: (**a**) the baseline period (1993–2014), (**b**) under the SSP1–2.6 scenario, and (**c**) under the SSP5–8.5 scenario for the future period (2015–2100). Gray bars indicate non-significant trends, blue bars indicate trends significant at the 5% level before FDR correction, and red bars indicate trends that remain significant after FDR correction

FDR correction, suggesting an intensification of heavy precipitation events and rainfall intensity under this scenario. However, indices such as R10mm, CDD, and CWD remain non-significant, indicating that changes in precipitation frequency and dry/wet spell duration are less pronounced. Under SSP1–2.6, temperature-related indices exhibit widespread and statistically significant changes. Warm extremes, including SU25, TR20, TX90p, TN90p, TXx, and TNx, show strong positive trends, while cold-related indices such as FD, TX10p, and TN10p show significant decreasing trends. These results indicate a coherent warming signal characterized by more frequent and intense warm extremes and a decline in cold events. Additionally, the growing season length (GSL) shows a significant increase, suggesting important implications for agriculture and ecosystem dynamics.

Under the high-emission SSP5–8.5 scenario, these patterns become more pronounced and, in some cases, more complex. Precipitation extremes show mixed behavior: Rx5day exhibits a significant increasing trend after FDR correction, while indices such as SDII, R95p, and R99p show weaker significance that does not persist after FDR adjustment. This suggests increased variability and uncertainty in precipitation responses under stronger forcing. In contrast, temperature extremes show a stronger and more consistent response compared to SSP1–2.6. Indices such as SU25, TR20, TXx, TNx, TXn, TNn, and GSL exhibit statistically significant trends after FDR correction, indicating substantial intensification of both warm extremes and seasonal changes. The frequency of cold events (FD) continues to decline significantly, while TX10p and TN10p also show decreasing tendencies, although their significance weakens after FDR correction. Notably, the diurnal temperature range (DTR) becomes significantly increasing under SSP5–8.5, suggesting differential warming between daytime and nighttime temperatures under stronger radiative forcing.

Across all scenarios, autocorrelation is generally weak for most indices; however, several temperature indices in future projections exhibit significant lag-1 autocorrelation, leading to reduced effective sample sizes. This highlights the importance of applying the modified Mann–Kendall approach to ensure robust trend detection.

In summary, while the baseline period reflects relatively stable extreme climate behavior with limited significant trends, future projections indicate a clear shift toward intensified extremes, particularly in temperature-related indices. The results consistently demonstrate that warming-driven changes—especially increases in warm extremes and reductions in cold events—are more robust and widespread than changes in precipitation extremes, with stronger signals under higher emission scenarios.

Uncertainty Analysis

To assess the uncertainty associated with projected changes in extreme climate indices, a bootstrap resampling approach was employed using 2000 iterations, a moving window size of 10 years, and a 95% confidence level. Uncertainty metrics including the average and maximum width of the 95% confidence interval (CI) and the d-factor were calculated for all indices under both SSP1–2.6 and SSP5–8.5 scenarios. Given the large number of indices (25 ETCCDI indices) and the inclusion of two future scenarios, only the uncertainty metrics (Table 7) and uncertainty plot of a representative index is presented in the main text (Fig. 8) for brevity, while the remaining plots are provided in the Supplementary Material (Fig. S5 and Fig. S6).

The results indicate that uncertainty levels vary substantially across different indices and between scenarios. In general, precipitation-related indices exhibit larger uncertainty compared to temperature-related indices. For instance, extreme precipitation indices such as R95p and R99p show the highest uncertainty ranges, with average 95% CI widths of 58.88 mm and 34.61 mm under SSP1–2.6, increasing to 63.59 mm and 34.46 mm under SSP5–8.5, respectively. Their maximum CI widths are also considerably large, reaching up to 119.96 mm for R95p under SSP5–8.5, indicating high variability and lower confidence in projections of extreme precipitation intensity. Similarly, indices such as Rx1day and Rx5day show notable increases in uncertainty under the high-emission scenario, reflecting the enhanced variability of short-duration extreme rainfall events.

In contrast, temperature-related indices generally exhibit lower uncertainty and more consistent behavior across scenarios. Indices such as TXx, TNx, TXn, and TNn show relatively small CI widths, indicating higher confidence in projections of temperature extremes. However, some temperature indices, particularly those related to percentile thresholds (e.g., TX90p and TN90p), show increasing uncertainty under SSP5–8.5, suggesting that the variability of extreme temperature occurrence may intensify under stronger radiative forcing.

The d-factor values further support these findings by quantifying the relative spread of uncertainty. Precipitation indices generally have higher d-factor values, particularly R20mm and R95p, indicating a wider spread of model outputs relative to observed variability. Conversely, indices such as CSDI and ID show very low d-factor values, suggesting limited variability and higher robustness in projections. Notably, the d-factor for several indices increases under SSP5–8.5, highlighting that uncertainty generally amplifies under higher emission scenarios.

Indices related to temperature extremes and heat events, such as SU25 and TR20, show moderate increases in

Table 7 Uncertainty metrics of ETCCDI extreme climate indices under SSP1–2.6 and SSP5–8.5 scenarios, including average and maximum width of 95% confidence intervals and d-factor derived from bootstrap analysis

Index	Unit	Avg 95% CI Width SSP1-2.6	Max 95% CI Width SSP1-2.6	d-factor SSP1-2.6	Avg 95% CI Width SSP5-8.5	Max 95% CI Width SSP5-8.5	d-factor SSP5-8.5
Rx1day	mm	13.35	24.83	1.12	14.81	36.92	1.24
Rx5day	mm	12.62	24.77	0.67	15.93	33.28	0.85
SDII	mm/day	1.52	2.42	1.28	1.53	2.33	1.28
R10mm	day	3.1	4.33	0.93	3.26	5.17	0.98
R20mm	day	2.09	3.33	1.6	2.21	3.5	1.69
CDD	day	24.7	37.85	1.11	27.24	38.5	1.22
CWD	day	0.93	1.27	1.02	1.01	2	1.1
R95p	mm	58.88	114.02	1.37	63.59	119.96	1.48
R99p	mm	34.61	85.68	1.18	34.46	71.55	1.17
SU25	day	6.38	10.57	0.67	7.91	14.55	0.83
TR20	day	5.32	8.71	0.62	7.63	15	0.9
TX90p	day	1.97	3.99	0.62	2.89	9.23	0.91
TN90p	day	2.02	4.93	0.49	3.28	11.87	0.8
WSDI	day	0.46	6.83	0.13	1.05	6.17	0.3
TXx	°C	0.68	2.82	0.55	0.9	2.85	0.73
TNx	°C	0.91	1.43	0.94	1.07	2.14	1.1
FD	day	5.92	23.33	0.48	5.01	23.33	0.41
ID	day	0.19	1.67	0.12	0.16	1.67	0.1
TXn	°C	1.34	3.28	0.68	1.45	3.3	0.74
TNn	°C	2.13	5.1	0.85	2.11	5.1	0.84
TX10p	day	2.33	6.5	0.54	2.93	8.69	0.67
TN10p	day	1.79	4.81	0.53	2.71	7.98	0.8
CSDI	day	0.2	3.5	0.04	0.2	3.5	0.04
DTR	°C	0.3	0.43	0.69	0.29	0.4	0.69
GSL	day	17.06	25.72	0.59	9.16	25.17	0.31

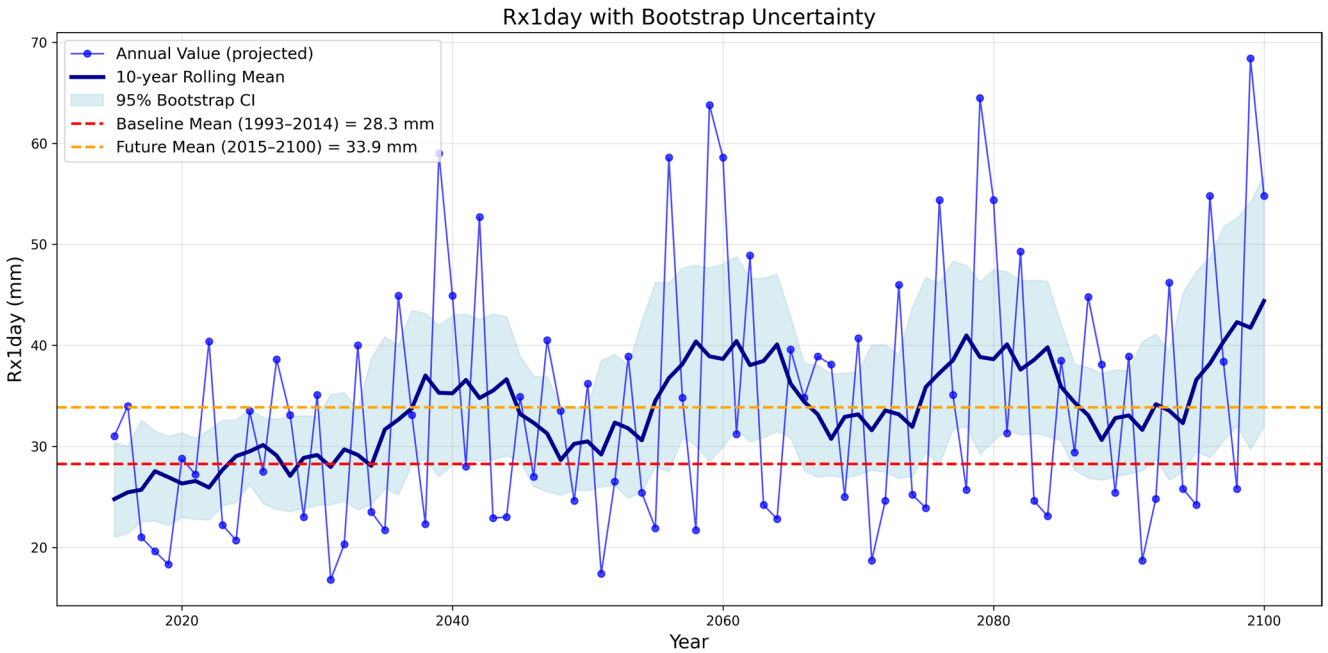

Fig. 8 Bootstrap-based uncertainty envelopes (95% confidence intervals) of Rx1day index under the SSP1-2.6 scenario

uncertainty under SSP5–8.5, consistent with the stronger warming signal and increased variability of heat extremes. Meanwhile, the growing season length (GSL) shows a relatively high uncertainty range under SSP1–2.6 but a lower average uncertainty under SSP5–8.5, suggesting a more consistent directional change under stronger forcing despite variability in magnitude.

Overall, the results demonstrate that uncertainty is systematically higher for precipitation extremes than for temperature extremes, and that uncertainty generally increases under the high-emission SSP5–8.5 scenario. This pattern reflects the inherently higher variability and model sensitivity associated with precipitation processes compared to temperature. These findings highlight the importance of considering uncertainty in interpreting future projections, particularly for extreme precipitation indices, where large variability may limit the robustness of projected changes.

Discussion

The projected changes in extreme climate indices for the Moghan Plain are broadly consistent with regional patterns documented in recent CMIP6-based studies over Western Asia and neighboring countries, while also revealing some sub-regional specificities that highlight local vulnerability.

Zareian et al. (2024) analyzed temperature and precipitation extremes across eight West Asian countries using a regional CMIP6 ensemble. They reported Tmax increases of +1.8 to +2.6 °C for Iran under SSP1-2.6 to SSP5-8.5, closely matching our projected warming in warm extremes (TXx +1.8 to +4.5 °C, TNx +1.1 to +3.0 °C) and sharp declines in cold extremes (FD: −23 to −36 days). Their P_{max} increase of +11 to +17% for Iran under SSP5-8.5 aligns with our intensified short-duration extremes (Rx1day: +5–6 mm, Rx5day: +1–3 mm) and heavy precipitation totals (R95p: +7–8 mm, R99p: +2–3 mm). They also noted TX90p increases of +3.1 to +10.1% for Iran under SSP5-8.5, supporting our projected rises in SU25, TR20, TX90p, and TN90p.

Usta et al. (2022) and Darand (2020) documented stronger warming over Iran relative to global averages, particularly under high-emission scenarios, consistent with our pronounced increases in warm extremes. Goodarzi et al. (2024) and Khansalari and Mohammadi (2024) projected increases in extreme precipitation intensity (R95p and AEPI) across Iran, with Khansalari and Mohammadi (2024) reporting an almost certain rise in R95p (up to 10%) under all scenarios and periods, aligning with our findings of heavier but less frequent rainfall events. Jiang et al. (2020) reported precipitation increases in Central Asia under high-emission scenarios, while Majdi et al. (2022) and Ali et al. (2023) highlighted rising temperature extremes and variable precipitation in the Middle East and Pakistan, supporting our results for warm indices and precipitation intensification.

Shahrezaei et al. (2026) found increasing minimum temperatures and variable precipitation along Iran's coasts, corroborating our decline in cold extremes. Hong et al. (2021) noted heterogeneous precipitation changes across Iran, with some regions showing no clear trend in R95p; however, our station-based results indicate consistent increases in R95p and related indices in the Moghan Plain, likely due to local orographic and convective effects. Tavosi et al. (2024) and Yousefi et al. (2024) projected intensified meteorological droughts under CMIP6 scenarios, aligning with our lengthening of dry spells (higher CDD). Also, multivariate risk assessments for rainfed agriculture have been conducted in semi-arid regions of Iran. For instance, a copula-based study in East Azerbaijan Province modeled the dependence between wheat yield and key climatic variables (precipitation, temperature, relative humidity), reporting below-average yield probabilities of 0.92–29.99% across 27 scenarios, with return periods ranging from 2 to 109 years (Allahverdipour and Fakheri-Fard 2026). These findings align with our observed high uncertainty in precipitation extremes and drought persistence in the Moghan Plain, particularly under SSP5-8.5, where prolonged CDD and intensified heavy rainfall events are projected.

Compared to neighboring countries, the magnitude of warming in the Moghan Plain (especially under SSP5-8.5) is similar to or slightly higher than the regional average for Iran, while precipitation intensification appears more pronounced than the multi-country ensemble means. This difference likely reflects local topographic and convective influences that amplify extreme rainfall intensity in the semi-arid lowlands of northern Iran, highlighting the vulnerability of this region to both prolonged drought and flash-flood risk.

These consistencies across multiple studies reinforce the robustness of the projected trends, while the differences underscore the value of high-resolution, station-based assessments for capturing sub-regional heterogeneity in Western Asia. Future research should continue to refine downscaling techniques and incorporate more local observations to better resolve such variations.

Conclusions

This study provides a comprehensive analysis and future projection of extreme temperature and precipitation indices in the Moghan Plain using eight CMIP6 global climate models under the SSP1-2.6 (low-emission) and SSP5-8.5

(high-emission) scenarios. The baseline period (1993–2014) was selected based on the availability of high-quality, homogenized observational data, and all model evaluations and future projections were consistently benchmarked against this 22-year period to ensure methodological coherence. Although shorter than the conventional 30-year climatological normal, this period remains statistically adequate for model validation and baseline characterization (Arguez et al. 2012).

The results indicate a clear shift toward more extreme climatic conditions in the coming decades. Precipitation patterns are projected to become more intense but less frequent, with increases in heavy rainfall indices (Rx1day, Rx5day, R95p, R99p, SDII, R10mm, R20mm) and a simultaneous lengthening of dry spells (higher CDD) and slight reduction in wet spells (lower CWD). These changes point to a deterioration in the temporal distribution of rainfall and an increased risk of hydrological stress. Temperature extremes show a strong warming signal: warm indices (TXx, TNx, SU25, TR20, TX90p, TN90p) are projected to rise significantly, while cold indices (FD, ID, TX10p, TN10p, CSDI) decline markedly. The growing season length (GSL) is expected to extend substantially (from 314.9 days to 335.6 and 352.1 days under SSP1-2.6 and SSP5-8.5, respectively), while the diurnal temperature range (DTR) remains relatively stable with only marginal increases. These projected changes are markedly stronger under the high-emission SSP5-8.5 pathway, underscoring the critical role of emission trajectories in determining the magnitude of future climate impacts.

This study is subject to several sources of uncertainty that should be considered when interpreting the results. First, inter-model variability introduces uncertainty, as different models may produce a range of responses due to differences in their structural formulations and parameterizations. This model spread reflects inherent uncertainties in representing complex climate and environmental processes. Second, the downscaling approach introduces additional uncertainty. The assumptions made during the downscaling procedure, including the stationarity of relationships between large-scale climate drivers and local-scale responses, may not fully capture future changes in regional climate dynamics. Third, uncertainty arising from emission scenarios (emission pathway variability) also plays a significant role. Different socio-economic pathways lead to substantially different forcing conditions, which in turn affect the magnitude and direction of projected changes. Finally, it should be noted that these uncertainties, along with other data and methodological limitations, may influence the precision of the results. Nevertheless, the overall patterns and conclusions of the study remain robust across the range of considered scenarios and models.

Overall, the Moghan Plain is projected to experience a hotter, more variable, and hydrologically stressed climate in the future. These findings highlight the urgent need for proactive adaptation strategies, including improved water management, heat-resilient crop varieties, adjusted agricultural calendars, enhanced early warning systems, and integrated land-use planning to build regional climate resilience.

While the present study provides a robust index-based assessment of climate extremes, it does not incorporate extreme value theory (e.g., GEV modeling or return period analysis) to quantify the probabilistic behavior of rare, high-impact events. Future work should expand the spatial scope (e.g., to watershed or provincial scales), integrate EVT-based approaches for tail risk characterization, and explore compound events (e.g., concurrent heat and drought) to support more comprehensive climate risk assessments and adaptation planning in the region.

This work contributes to a better understanding of future climate risks in the Moghan Plain and underscores the importance of aligning mitigation and adaptation efforts with the projected intensification of extremes under different emission pathways.

Supplementary Information The online version contains supplementary material available at https://doi.org/10.1007/s12145-026-02131-9.

Author contributions All authors contributed to the study conception, methodology development, data collection, and results validation. P.A. Provided software, created visualizations, conducted investigation, and performed formal analysis. Y.D. administered the project, performed formal analysis, and supervised research. The first draft of the manuscript was written by P.A., and all authors commented on previous versions of the manuscript. All authors read and approved the final manuscript.

Funding The authors declare that no funds, grants, or other support were received during the preparation of this manuscript.

Data availability The meteorological data were downloaded from the Iranian Meteorological Organization (https://data.irimo.ir). Data sets used during the current study are available from the corresponding author on reasonable request.

Declarations

Competing interests The authors declare no competing interests.

References

Aleshina MA, Semenov VA, Chernokulsky AV (2021) A link between surface air temperature and extreme precipitation over Russia from station and reanalysis data. Environ Res Lett 16(10):105004. https://doi.org/10.1088/1748-9326/ac1cba

Ali Z, Hamed MM, Muhammad MK, Iqbal Z, Shahid S (2023) Performance evaluation of CMIP6 GCMs for the projections of

precipitation extremes in Pakistan. Clim Dyn 61:4717–4732. https://doi.org/10.1007/s00382-023-06831-6

Allahverdipour P, Fakheri-Fard A (2026) Copula-based mapping of compound climate risks to rainfed wheat yield in Semi-Arid Iran. Earth Syst Environ 1–27. https://doi.org/10.1007/s41748-026-01080-z

Arguez A, Durre I, Applequist S, Vose RS, Squires MF, Yin X, Heim RR Jr, Owen TW (2012) NOAA's 1981–2010 US climate normals: an overview. Bull Am Meteorol Soc 93(11):1687–1697. https://doi.org/10.1175/BAMS-D-11-00197.1

Benjamini Y, Hochberg Y (1995) Controlling the false discovery rate: a practical and powerful approach to multiple testing. J R Stat Soc B 57(1):289–300. https://doi.org/10.1111/j.2517-6161.1995.tb02031.x

Cannon AJ, Sobie SR, Murdock TQ (2015) Bias correction of GCM precipitation by quantile mapping: how well do methods preserve changes in quantiles and extremes? J Clim 28(17):6938–6959. https://doi.org/10.1175/JCLI-D-14-00754.1

Chen H, Sun J, Lin W, Xu H (2020) Comparison of CMIP6 and CMIP5 models in simulating climate extremes. Sci Bull 65(17):1415–1418. https://doi.org/10.1016/j.scib.2020.05.015

Chen S, Wu R, Chen W (2019) Projections of climate changes over mid-high latitudes of Eurasia during boreal spring: uncertainty due to internal variability. Clim Dyn 53(9):6309–6327. https://doi.org/10.1007/s00382-019-04929-4

Choudhary S, Pingale SM, Khare D, Patidar R, Krishan R (2025) Comprehensive evaluation of precipitation reanalysis products and CMIP6 models using statistical and machine learning techniques with nature-inspired optimization. Intl J Climatol 46:e70159. https://doi.org/10.1002/joc.70159

Darand M (2020) Future changes in temperature extremes in climate variability over Iran. Meteorol Appl 27(6):e1968. https://doi.org/10.1002/met.1968

Dinpashoh Y, Allahverdipour P (2025) Monitoring and predicting changes in reference evapotranspiration in the Moghan Plain according to CMIP6 of IPCC. Environ Water Eng 11(1):47–56. https://doi.org/10.22034/ewe.2024.466037.1947

Dinpashoh Y, Jhajharia D, Fakheri-Fard A, Singh VP, Kahya E (2011) Trends in reference crop evapotranspiration over Iran. J Hydrol 399:422–433. https://doi.org/10.1016/j.jhydrol.2011.01.021

Elliot T, Torres-Matallana JA, Teebken J (2025) Urbanization under extreme climate events leads to synchronized decreases in flood protection and increases in vulnerability. Cities 160:105827. https://doi.org/10.1016/j.cities.2025.105827

Fathian F, Ghadami M, Dehghan Z (2023) Spatial analysis of extreme temperature indices under climate change based on CORDEX data and a developed Bias correction method in Iran. J Water Soil Sci 26(4):137–160. https://doi.org/10.47176/jwss.26.4.15012

Felix ML, Kim YK, Choi M, Kim JC, Do XK, Nguyen TH, Jung K (2021) Detailed trend analysis of extreme climate indices in the Upper Geum River Basin. *Water*. 13 (22): 3171. https://doi.org/10.3390/w13223171

Goodarzi MR, Abedi MJ, Niazkar M (2024) Effects of climate change on streamflow in the Dez Basin of Iran using the IHACRES model based on the CMIP6 model. J Water Clim Change 15(6):2595–2611. https://doi.org/10.2166/wcc.2024.571

Grazzini F, Craig GC, Keil C, Antolini G, Pavan V (2020) Extreme precipitation events over northern Italy. Part I: A systematic classification with machine-learning techniques. Q J R Meteorolog Soc 146(726):69–85. https://doi.org/10.1002/qj.3635

Hamed KH, Rao AR (1998) A modified Mann-Kendall trend test for autocorrelated data. J Hydrol 204(1–4):182–196. https://doi.org/10.1016/s0022-1694(97)00125-x

Haynes W (2013) Benjamini–Hochberg Method. In: Dubitzky W, Wolkenhauer O, Cho KH, Yokota H (eds) Encyclopedia of Systems Biology. Springer, New York, NY. https://doi.org/10.1007/978-1-4419-9863-7_1215

Hong J, Javan K, Shin Y, Park JS (2021) Future Projections and Uncertainty Assessment of Precipitation Extremes in Iran from the CMIP6 Ensemble. Atmos 12(8):1052. https://doi.org/10.3390/atmos12081052

IPCC (2013) Climate Change 2013: The Physical Science Basis. Contribution of Working Group I to the Fifth Assessment Report of the Intergovernmental Panel on Climate Change. Cambridge University Press, Cambridge, United Kingdom and New York, NY, USA, p 1535. https://www.ipcc.ch/report/ar5/wg1/

Jiang J, Zhou T, Chen X, Zhang L (2020) Future changes in precipitation over Central Asia based on CMIP6 projections. Environ Res Lett 15(5):054009. https://doi.org/10.1088/1748-9326/ab7d03

Karl TR, Nicholls N, Ghazi A (1999) CLIVAR/GCOS/WMO Workshop on Indices and Indicators for Climate Extremes Workshop Summary. Weather and Climate Extremes. Springer, Dordrecht. https://doi.org/10.1007/978-94-015-9265-9_2

Kendall MG (1948) Rank correlation methods. Charles Griffin, London

Khansalari S, Mohammadi A (2024) Probabilistic projection of extreme precipitation changes over Iran by the CMIP6 multi-model ensemble. Clim Change 177:115. https://doi.org/10.1007/s10584-024-03771-w

Kouzegaran S, Mousavi Baygi M, Babaeian I (2021) Temperature extreme indices projection based on RCP scenarios in Northeast of Iran. Water Soil 34(6):1351–1366. https://doi.org/10.22067/jsw.v34i6.85845

Kuinkel D, Promchote P, Upreti KR, Wang SYS, Dahal N, Pokharel B (2024) Projected changes in precipitation extremes in Southern Thailand using CMIP6 models. Theor Appl Climatol 155(9):8703–8716. https://doi.org/10.1007/s00704-024-05150-y

Majdi F, Hosseini SA, Karbalaee A, Kaseri M, Marjanian S (2022) Future projection of precipitation and temperature changes in the Middle East and North Africa (MENA) region based on CMIP6. Theor Appl Climatol 147:1249–1262. https://doi.org/10.1007/s00704-021-03916-2

Mann HB (1945) Nonparametric tests against trend. Econometrica 13(3):245–259. https://doi.org/10.2307/1907187

Mohamadi N, Sari Saraf B, Rostamzadeh H (2023) Trend investigation and spatial analysis of Warm and Cold spells duration index based on SSPs scenarios in northwest of Iran. J Spat Anal Environ Hazards 10(3):183–204. https://doi.org/10.61186/jsaeh.10.3.183

Peterson T, Folland C, Gruza G, Hogg W, Mokssit A, Plummer N (2001) Report on the activities of the working group on climate change detection and related rapporteurs. World Meteorological Organization, Geneva

Rajkumar GA, Nema MK, Khare D (2026) Spatiotemporal assessment of extreme rainfall events in the Wainganga River basin using CMIP6 climate models. Nat Hazard 122(6):250. https://doi.org/10.1007/s11069-026-08018-8

Sarkar S, Maity R (2022) Future characteristics of extreme precipitation indicate the dominance of frequency over intensity: a multi-model assessment from CMIP6 across India. J Geophys Res Atmos 127:e2021JD035539. https://doi.org/10.1029/2021JD035539

Semenov MA (2021) LARS-WG stochastic weather generator. https://doi.org/10.5281/zenodo.4572752. Zenodo

Semenov MA, Senapati N, Coleman K, Collins AL (2025) A dataset of large ensemble of CMIP6-based transient climate scenarios for impact assessment in Great Britain. Data Brief 111695. https://doi.org/10.1016/j.dib.2025.111695

Sen PK (1968) Estimates of the regression coefficient based on Kendall's tau. J Am Stat Assoc 63(324):1379–1389. https://doi.org/10.1080/01621459.1968.10480934

Shahrezaei FP, Alavinia S, Omidvar E (2026) Projections of future climates: exploring temperature and precipitation patterns in

Iran's coastal regions with MPI-ESM1.2-HR. J Earth Syst Sci 135:38. https://doi.org/10.1007/s12040-026-02738-y

Shenoy S, Gorinevsky D, Trenberth KE, Chu S (2022) Trends of extreme US weather events in the changing climate. *Proc. Natl. Acad. Sci.* 119 (47): e2207536119. https://doi.org/10.1073/pnas.2207536119

Sun Q, Zhang X, Zwiers F, Westra S, Alexander LV (2021) A global, continental, and regional analysis of changes in extreme precipitation. J Clim 34(1):243–258. https://doi.org/10.1175/JCLI-D-19-0892.1

Tavosi M, Vafakhah M, Shekohideh H, Sadeghi SH, Moosavi V, Zheng Z, Yang Q (2024) Rainfall Extreme Indicators Trend and Meteorological Drought Changes Under Climate Change Scenarios. Water Resour Manage 38:4393–4413. https://doi.org/10.1007/s11269-024-03871-3

Tefera GW, Ray RL, Wootten AM (2024) Evaluation of statistical downscaling techniques and projection of climate extremes in central Texas, USA. Weather Clim Extremes 43:100637. https://doi.org/10.1016/j.wace.2023.100637

Usta DFB, Teymouri M, Chatterjee U (2022) Assessment of temperature changes over Iran during the twenty-first century using CMIP6 models under SSP1-26, SSP2-4.5, and SSP5-8.5 scenarios. Arab J Geosci 15:416. https://doi.org/10.1007/s12517-022-09709-9

Wang Y, Bai X, Lei Y, Ding W, Wu S (2025) The Projection of Extreme Heat and Precipitation Events in China Response to Global Warming Under the SSP1-2.6 and SSP5-8.5 Scenarios. Int J Climatol e8807. https://doi.org/10.1002/joc.8807

Wei L, Xin X, Li Q, Wu Y, Tang H, Li Y, Yang B (2023) Simulation and projection of climate extremes in China by multiple Coupled Model Intercomparison Project Phase 6 models. Int J Climatol 43(1):219–239. https://doi.org/10.1002/joc.7751

Yousefi H, Ahani A, Moridi A, Razavi S (2024) The future of droughts in Iran according to CMIP6 projections. Hydrol Sci J 69(7):951–970. https://doi.org/10.1080/02626667.2024.2348720

Yu B, Li G, Chen S, Lin H (2020) The role of internal variability in climate change projections of North American surface air temperature and temperature extremes in CanESM2 large ensemble simulations. Clim Dyn 55(3):869–885. https://doi.org/10.1007/s00382-020-05296-1

Zareian MJ, Dehban H, Gohari A (2024) Changes in temperature and precipitation extremes over Western Asia: a regional ensemble from CMIP6. Atmos Res 311:107707. https://doi.org/10.1016/j.atmosres.2024.107707

Zhang X, Yang F (2004) RClimDex (1.0) user manual. Clim Res Branch Environ Can 22:13–14

Zhu R, Wu X, Zhang W, He J, Qin Y, Li Z, Shen Y (2024) Seasonally extreme temperature events accelerate in arid northwestern China during 1979–2018. Atmos Res 300:107230. https://doi.org/10.1016/j.atmosres.2024.107230